MULTI-BASELINE GRAVITATIONAL WAVE RADIOMETRY

By

DIPONGKAR TALUKDER

A thesis submitted in partial fulfillment of
the requirements for the degree of

Master of Science in Physics

WASHINGTON STATE UNIVERSITY
Department of Physics and Astronomy

December 2008

To the Faculty of Washington State University:

The members of the Committee appointed to examine the dissertation of DIPONGKAR TALUKDER find it satisfactory and recommend that it be accepted.

_____
Chair

_____

_____

ACKNOWLEDGEMENT

First of all, I would like to express my gratitude and warm-hearted thanks to Sukanta Bose, without whose ceaseless inspiration, kind co-operation and valuable advice, it would be quite impossible on my part to accomplish such a hard work. I would have been lost without his great efforts to motivate me in a new branch of physics, gravitational wave research.

I am deeply obliged to Bruce Allen for his support and hospitality during my stay at Albert Einstein Institute, Hannover, Germany.

My sincere thanks to Sanjit Mitra and Stefan Ballmer for their co-operation and helpful discussions. It would not be possible for me to write this thesis without their primary work on this promising idea.

I am delighted to interact with the people in LIGO-Virgo scientific collaboration. I take this opportunity to thank my friends in Washington State University and Albert Einstein Institute for their friendship and entertainment. Special thanks to Holger Pletsch for providing me a nice map-making tool.

I cannot end without thanking my family for their encouragement and providing a loving environment for me. To them I dedicate my thesis.

MULTI-BASELINE GRAVITATIONAL WAVE

RADIOMETRY

Abstract

by Dipongkar Talukder, M.S.
Washington State University
December 2008

Chair: Sukanta Bose

We consider the maximum likelihood (ML) statistic for detecting an anisotropic astrophysical stochastic gravitational-wave background with multiple interferometric baselines. For any given baseline, we establish a formalism for constructing an orthonormal pixel basis in sky positions utilizing the knowledge of the point-spread function for that baseline. The ML statistic for a single baseline is then just the excess power in that orthonormal basis. An analogous formulation of the ML statistic is available for a spherical harmonic basis and lays the ground-work for a systematic comparison between the effectiveness of pixel-based and spherical-harmonic-based deconvolution techniques for a variety of stochastic source distributions. The sensitivities of three different baselines and their network for single- and multi-pixel sources are compared here. For detector noise that is Gaussian and uncorrelated across baselines, the network sensitivity-squared is the sum of the squares of the individual baseline sensitivities, analogous to what was found before for the network signal-to-noise ratio (SNR) of the "optimal filter" statistic for an isotropic stochastic gravitational wave background. Also, the accuracies with which a single-pixel

source can be located with the separate baselines and their network are obtained and compared using the Fisher information matrix.

Contents

List of Figures

Chapter 1

Preface

Just like the discovery of the cosmic microwave background and pulsars in the electromagnetic spectrum, a discovery of unknown sources by earth-based detectors such as LIGO [21] and Virgo [22] in the gravitational wave (GW) spectrum by serendipity is an interesting prospect. The LIGO Scientific Collaboration [23] is addressing it by searching for both transient signals, or "bursts", and long-duration ones in LIGO-Virgo data. Here we focus on a subset of the latter type of signals that can be modeled as a stochastic background arising, e.g., from an unresolved superposition of GW signals from multiple sources, such as low-mass X-ray binaries (LMXBs) or, even, coalescing compact objects in advanced detector configurations [5].

Our aim is to (1) find the optimal statistic for detecting an astrophysical GW background (AGWB) with a single baseline, (2) extend it for multiple baselines, (3) compare their sensitivities to different sky positions for the LIGO-Virgo baselines, and (4) compare the accuracies with which a single-pixel source can be located with the separate baselines and their network. In the process, we establish a formal-

ism in which the effectiveness of pixel- and spherical-harmonic-based deconvolution techniques for obtaining source sky-maps can be compared for different source distributions.

The thesis has been organized as follows: Chapter 2 provides an introduction to gravitational waves as well as a description of earth-based interferometric detectors and gravitational-wave sources detectable by them. An introduction to stochastic gravitational waves background and its statistical properties are provided in Chapter 3. A detailed review of the general radiometer analysis for the detection of anisotropic stochastic background is given in Chapter 4. The issues of detection statistic and parameter accuracies for AGWB are mainly addressed here. We develop a formalism for combining the output of a network of baselines as well. A Fisher information matrix calculation for assessing the accuracy with which a network can locate a single-pixel source is provided too. Implementation of multi-baseline radiometer techniques is also presented in this chapter. Finally, the summary of the main results obtained in this thesis and future directions are discussed in Chapter 5.

Chapter 2

Gravitational Waves

In 1916, Albert Einstein published his famous Theory of General Relativity (GR). Einstein's general theory describes how massive object affects curvature of space and time. Gravitational wave is a fluctuation in the curvature of space-time which propagates with the speed of light. It transports energy and momentum. When two massive objects, like neutron stars, orbit each other, space-time is stirred by their motion, and gravitational radiation ripples outward into the universe.

In General Relativity, the lowest multipole that produces gravitational waves is the quadrupole moment. Gravitational waves (GWs) decrease in strength as inverse of the distance as they move away from the source. Owing to their weak interaction with matter, GWs travel large distances with negligible absorption or distortion. Detection of gravitational waves is not only important to test GR, but promises a new window for GW astronomy. This gives rise to the expectation that the detection of gravitational waves will reveal a new view of the universe. It will tell us about the dynamics of large-scale events in the universe like the death of stars, and the

birth of black holes.

2.1 Gravitational waves (GWs) in general relativity

In this work, we adopt the following notation: The space-time coordinates are given by $x^\mu := (x^0, x^i) = (x^0, x^1, x^2, x^3) = (ct, x, y, z)$ and $x_\mu := (x_0, x_i) = (-x^0, x^i)$. While the *Greek indices* (e.g. μ, ν) assume space-time indices $(0, 1, 2, 3)$, the Latin indices (e.g. i, j) run over three spatial coordinate labels, $1, 2, 3$ or x, y, z. The partial derivatives with respect to the coordinates are abbreviated using the symbols $\partial_\mu = \partial/\partial x^\mu$ and $\partial^\mu = \partial/\partial x_\mu$. We also define a comma-notation to indicate derivatives, i.e., $\partial_\beta f \equiv f_{,\beta}$ and $\partial^\beta f \equiv f^{,\beta}$. Repeated indices are summed over unless otherwise indicated.

The curved space-time is best described in Riemannian manifolds [6] by a dynamical field $g_{\mu\nu}$, which is a function of the space-time coordinates x^μ. The infinitesimal proper distance $d\tau$ between two space-time events separated by coordinate distance dx^μ is given by

$$d\tau^2 = g_{\mu\nu} dx^\mu dx^\nu, \tag{2.1}$$

where the Einstein summation convention is understood on the right hand side. In the limit of flat space-time, the metric $g_{\mu\nu}$ becomes the Minkowski metric $\eta_{\mu\nu} = \text{diag}(-1, 1, 1, 1)$.

The curvature and dynamics of space-time governed by the distribution and

kinematics of energy are expressed geometrically by the Einstein equation (EE):

$$G_{\mu\nu}(g) = \frac{8\pi G}{c^4} T_{\mu\nu} \ , \tag{2.2}$$

where $G_{\mu\nu}$ is the Einstein tensor, G is Newton's constant and $T_{\mu\nu}$ is known as the stress tensor. Due to its nonlinearity, a complete description of the solutions of EE is not yet possible. One class of solutions to the EE is obtained in the linearized theory close to flat space-time, i.e., where fields are everywhere weak.

In weak gravity, the metric is approximately Minkowskian and can be decomposed into the flat space-time metric plus a small perturbation,

$$g_{\mu\nu} = \eta_{\mu\nu} + h_{\mu\nu} \ , \quad |h_{\mu\nu}| \ll 1. \tag{2.3}$$

The most general coordinate transformation of the form

$$x^\mu \rightarrow x^\mu + \xi^\mu(x) \ , \quad |\xi^\mu_{,\nu}| \ll 1, \tag{2.4}$$

preserves the form of the metric given by (2.3) if the perturbations are transformed using the formula

$$h_{\mu\nu} \rightarrow h_{\mu\nu} - \xi_{\mu,\nu} - \xi_{\nu,\mu} \ . \tag{2.5}$$

To see the physical effect of a gravitational wave it is useful to choose a gauge. The Lorentz gauge freedom allows us to choose a coordinate system where the trace-reversed metric perturbations,

$$\bar{h}_{\mu\nu} := h_{\mu\nu} - \frac{1}{2} \eta_{\mu\nu} h^\alpha_\alpha \ , \tag{2.6}$$

are divergence free,

$$\bar{h}_{\mu\nu}{}^{,\nu} = 0. \tag{2.7}$$

5

This reduces the Einstein field equation to a simple wave equation:

$$\Box \bar{h}_{\mu\nu} = -\frac{16\pi G}{c^4} T_{\mu\nu} \,, \tag{2.8}$$

where $\Box$ denotes the d'Alembertian operator:

$$\Box := \partial_\mu \partial^\mu = -\frac{1}{c^2}\frac{\partial^2}{\partial t^2} + \nabla^2. \tag{2.9}$$

We now focus on a region of space outside the source where all the components of the stress-energy tensor are zero, i.e.,

$$\Box \bar{h}_{\mu\nu} = 0. \tag{2.10}$$

This allows us to impose the transverse-traceless (TT) gauge, defined by the conditions:

$$
\begin{aligned}
h_{\mu\nu}{}^{,\nu} &= 0 \quad \text{(transverse)} \,, \\
h_\mu{}^\mu &= 0 \quad \text{(traceless)} \,,
\end{aligned}
\tag{2.11}
$$

which assures that the trace-reversed perturbation $\bar{h}_{\mu\nu}$ is identical to the physical perturbation $h_{\mu\nu}$.

The effect of a gravitational wave on a test mass in space can be found by looking at a plane wave solution of equation (2.10) under TT gauge with wave vector k_σ:

$$h_{\mu\nu}(x) = A_{\mu\nu} e^{ik_\alpha x^\alpha} \,, \tag{2.12}$$

with $k_\alpha k^\alpha = 0$ and $A_{\mu\nu} k^\nu = A_\mu{}^\mu = 0$. Choosing the wave vector k_i along the z-axis, one can completely parametrize the amplitude $A_{\mu\nu}$ by two independent polarizations,

6

h_+ and $h_\times$:

$$A_{\mu\nu} := \begin{pmatrix} 0 & 0 & 0 & 0 \\ 0 & h_+ & h_\times & 0 \\ 0 & h_\times & -h_+ & 0 \\ 0 & 0 & 0 & 0 \end{pmatrix}. \tag{2.13}$$

A gravitational wave with h_+ polarization stretches distance along x-axis and shortens distance along y-axis during the first half cycle and does the opposite during the the second half cycle. The $h_\times$ polarization does the same thing, but in a coordinate system rotated by 45 degree. Figure 2.1 shows the effect of a gravitational wave on a ring of particles.
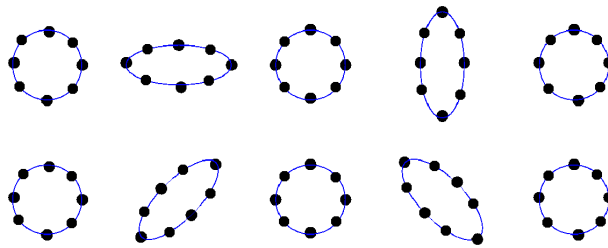

Figure 2.1: The effect of the two polarizations h_+ (*top panel*) and $h_\times$ (*bottom panel*) of a complete cycle of sinusoidal gravitational wave propagating through the page on a ring of test particles.

2.2   Principle of a GW detector

In a nutshell a laser interferometric gravitational-wave detector is a sensitive interferometer that measures the change in relative spatial distance of suspended test masses induced by an impinging gravitational wave. Figure 2.2 is a schematic of an

earth-based laser interferometric detector. The basic principle on which a detector works is that of interference of light waves. Each of the two orthogonal arms of the interferometer contains a pair of mirrored test masses which form a Fabry-Perot optical cavity [7]. Laser light is divided at the beam splitter, and reflected from the cavities in each arm. This reflected light acquires a phase shift which is very sensitive to the separations of the test masses. These phase shifts are then compared when the light recombines at the beam splitter. If there is an impinging gravitational wave it will act to stretch or squeeze the surrounding space-time, effectively causing distances to shrink in one arm while stretching in the other. This then leads to an overall phase difference in the light of the two arms.
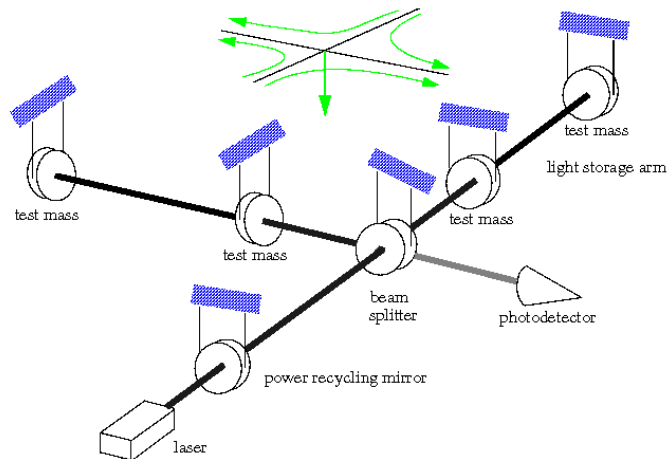

Figure 2.2: Simplified schematic of an earth-based interferometric detector.

Suppose the interferometer in Fig. 2.2 is arranged such that its arms lie along the x and y axes. Suppose further that test masses are separated by a distance L along the arms. When a gravitational wave with polarization h_+ passes through the

8

interferometer, the separation between the two masses in the x arm is given by

$$L_x(t) = \sqrt{L\, g_{xx}\, L} \approx \left(1 + \frac{h_+(t)}{2}\right) L \ , \tag{2.14}$$

whereas, in the y arm,

$$L_y(t) \approx \left(1 - \frac{h_+(t)}{2}\right) L \ . \tag{2.15}$$

The wave is thus detectable by measuring the length difference between two arms. The difference in length of the two arms is given by

$$\frac{\delta L(t)}{L} := \frac{L_x(t) - L_y(t)}{L} = h_+(t) \ . \tag{2.16}$$

Generally, both polarizations of the wave influence the test masses and hence,

$$\frac{\delta L(t)}{L} = F^+ h_+(t) + F^\times h_\times(t) \equiv h(t), \tag{2.17}$$

where F^+ and $F^\times$ are antenna response functions, which depend on the source location and their orientation, which changes with time, on the globe. Since a gravitational wave induces a strain in the detector, $h(t)$ is often referred to as the "gravitational wave strain".

The principal noise sources affecting interferometer sensitivity are background motions of the test masses, mainly due to seismic noise, thermal noise, and noise in sensing the test mass motion due to laser noise, quantum fluctuations of the light, and fluctuations in the number of residual gas molecules traversing the optical beams.

Figure 2.3 shows, along with the noise $\tilde{n}(f)$ curves, the estimated signal strengths $\tilde{h}(f)$ for various sources. The signal strength $\tilde{h}(f)$ is defined in such a way that, wherever a signal point or curve lies above the interferometer's noise curve, the signal, coming from a random direction on the sky and with a random orientation, is detectable with a false alarm probability of less than one percent.
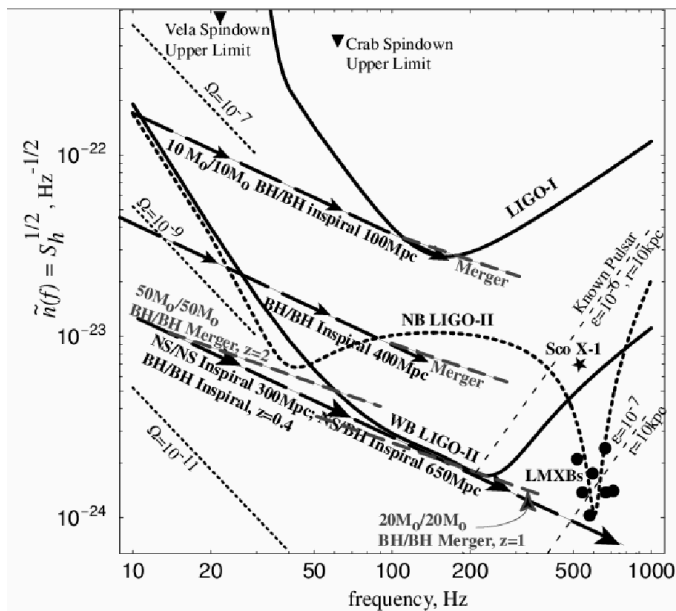
Figure 2.3: The noise $\tilde{n}(f)$ in several stages of LIGO interferometers plotted as a function of gravitational wave frequency f, and compared with the estimated signal strengths $\tilde{h}(f)$ from various sources [12].

2.3 Sources of gravitational waves

There are different kinds of "known" and "unknown" sources which generate GW with different frequency spectra. Interferometric gravitational wave detectors have achieved unprecedented sensitivity to gravitational waves, expected from astrophysical sources of different kinds:

Burst: Brief transients from violent events like coalescing compact binary, composed of massive neutron stars and/or black holes and asymmetrical core collapse

10

in supernovae are in this category. Core collapse in massive stars has long been regarded as likely to be an important source of gravitational waves.

Continuous: Periodic sources like pulsars and inspiraling binaries which emit GW continuously over a long duration without significant change in their characteristics are called continuous sources.

Stochastic: Stochastic backgrounds of gravitational waves produced by superposition of a large umber of independent, uncorrelated astrophysical and cosmological origin that are not individually resolvable.

Depending on source characterizations, there exists several search methods. The GW signals from compact coalescing binaries have been "precisely" modeled using post-Newtonian approximations, hence matched filtering technique is used for extracting the true GW signal buried inside strong detector noise. A targeted search, by correlating signals from two detectors with a time dependent phase factor that accounts for the light travel time delay between two detectors, is the best strategy for the detection of GW from known radio pulsars. Since the stochastic signals are unmodeled, the best strategy to detect stochastic sources is by correlating outputs of two detectors with appropriate time delays.

Chapter 3

Stochastic GW Background

The universe is expected to have Stochastic Gravitational Wave Backgrounds (SG-WBs) of astrophysical and cosmological origin. Incoherent superposition of un-modeled and/or unresolved sources of GWs contributing to the detectors' output constitute a SGWB [11].

In the early universe inflation produces a stochastic background of gravitational waves through the parametric amplification of primordial quantum fluctuations [9]. Unfortunately this background itself is too weak to be directly detected with existing ground-based detectors. In the period following inflation there are a number of mechanisms that may have operated to produce additional SGWB from inhomogeneities in the fields that populate the early universe. For example, first-order phase transitions in the early universe can generate a stochastic background of gravitational waves that may be detectable today [10].

In addition to the cosmological background, an astrophysical contribution may have resulted from the superposition of a large number of unresolved astrophysical
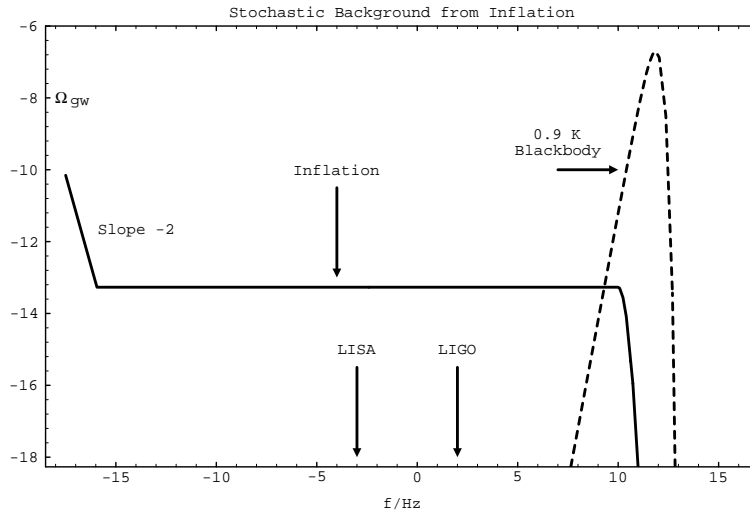
Figure 3.1: The spectrum of stochastic gravitational waves in inflationary models is flat over a wide range of frequencies, and is shown as the solid curve [11]. The horizontal axis is $\log_{10}$ of frequency, in Hz. The vertical axis is $\log_{10} \Omega_{\mathrm{gw}}$ define in (3.8).

sources, whose frequency is expected to evolve very slowly compared to the observation time [5]. These can be either short-lived burst sources, such as stellar core collapses to neutron stars or black holes, phase transition or oscillation modes in young neutron stars, the final stage of compact binary mergers, or periodic long-lived sources, typically pulsars, the early inspiral phase of compact binaries or captures by supermassive black holes.

Figure 3.1 shows the spectrum of a SGWB predicted by inflationary models to exist today over a wide range of frequencies. The inflationary spectrum rises rapidly at low frequencies and falls off above the frequency scale f_{max} associated with the
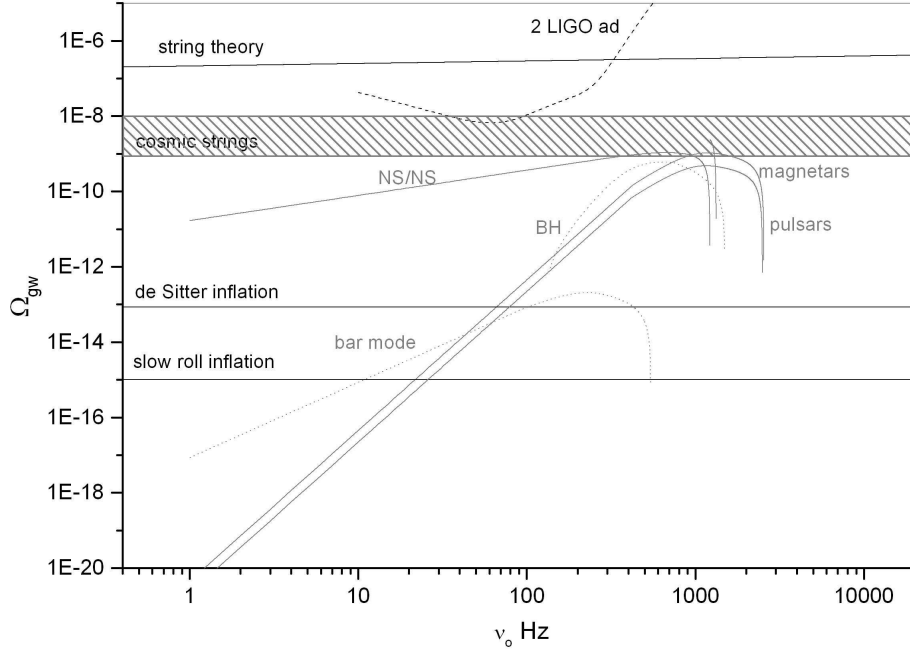
Figure 3.2: Gravitational wave spectrum as a function of observed frequency for potential SGWB sources from astrophysical origin [5].

fastest characteristic time of the phase transition at the end of inflation. Because the spectrum falls off as inverse to the square of frequency at low frequencies, this is certainly too small to be detectable with either initial or advanced LIGO.

Figure 3.2 shows the gravitational wave spectra plotted as a function of observed frequency for potentially significant AGWBs and their detectability using the two upcoming advanced LIGO detectors. The detectability of an AGWB is determined by the detector sensitivity, which sets the detection horizon. As the sensitivity of LIGO improves and the next generation of GW observatories come on line, it is

plausible that AGWBs can be observed for the first time, providing new insight into both the sources generating them and the evolutionary history of the Universe.

It is well established that the cosmic microwave background (CMB) is isotropic. But the assumption of isotropy for SGWB may not be true. For example, if the dominant source of stochastic gravitational waves in the frequency band of the earth-based detectors comes from an ensemble of astrophysical sources mentioned above, then the stochastic background will have a distinctly *anisotropic* distributions. The AGWB is of major interest in this thesis.

3.1 The detector strain due to a SGWB

In the transverse traceless gauge, the metric perturbations due to a stochastic gravitational-wave background can be written as a superposition of plane waves

$$h_{ab}(t, \mathbf{x}) = \int_{-\infty}^{\infty} df \int_{S^2} d\hat{\Omega} \; e_{ab}^A(\hat{\Omega}) \; \tilde{h}_A(f, \hat{\Omega}) e^{i2\pi f(t+\hat{\Omega}\cdot\mathbf{x}/c)} \; , \qquad (3.1)$$

where $e_{ab}^A(\hat{\Omega})$ are the gravitational-wave polarization tensors, $\hat{\Omega}$ is a unit vector pointing in the direction of wave propagation and summation over polarization indices $A = \{+, \times\}$ is understood. Since the GW strain $h_{ab}(t, \mathbf{x})$ is real, the complex Fourier amplitudes $\tilde{h}_A(f, \hat{\Omega})$ satisfy $\tilde{h}_A(-f, \hat{\Omega}) = \tilde{h}_A^*(f, \hat{\Omega})$.

In standard angular coordinates on the two-sphere $\theta \in [0, \pi]$, $\phi \in [0, 2\pi]$, one can write

$$\begin{aligned}
\hat{\Omega} &= \sin\theta\cos\phi\,\hat{x} + \sin\theta\sin\phi\,\hat{y} + \cos\theta\,\hat{z} \; , \\
\hat{m} &= \cos\theta\cos\phi\,\hat{x} + \cos\theta\sin\phi\,\hat{y} - \sin\theta\,\hat{z} \; , \\
\hat{n} &= -\sin\phi\,\hat{x} + \cos\phi\,\hat{y} \; , \qquad\qquad (3.2)
\end{aligned}$$

so that $\{\hat{m}, \hat{n}, \hat{\Omega}\}$ form a right-handed system of unit vectors. The axes are defined as follows: for a fixed but arbitrarily chosen origin of time $t = 0$, $\hat{x}$ is directed towards the intersection of the equator and the longitude $\phi = 0$, $\hat{z}$ points along the North Celestial Pole and $\hat{y}$ is chosen orthogonal to the previous two exes forming a right-handed triad. The the polarization tensors $e_{ab}^A(\hat{\Omega})$ are defined by the following expressions:

$$
\begin{aligned}
e_{ab}^+(\hat{\Omega}) &= \hat{m}_a\hat{m}_b - \hat{n}_a\hat{n}_b , \\
e_{ab}^\times(\hat{\Omega}) &= \hat{m}_a\hat{n}_b - \hat{n}_a\hat{m}_b .
\end{aligned}
\tag{3.3}
$$

We consider the Ith GW detector to be located at $\mathbf{x}_I(t)$. We also take $\hat{X}_I(t)$, $\hat{Y}_I(t)$ as unit vectors pointing along the interferometer arms for detector I. These three detector location vectors and orientation are all time-dependent due to the earth's rotation. Then the detector tensor is given by

$$
d_I^{ab}(t) = \frac{1}{2}\left[\hat{X}_I^a(t)\,\hat{X}_I^b(t) - \hat{Y}_I^a(t)\,\hat{Y}_I^b(t)\right] ,
\tag{3.4}
$$

and the strain $h_I(t)$ in the Ith detector is given by

$$
h_I(t) = h_{ab}(t, \mathbf{x}_I(t))\, d_I^{ab}(t) .
\tag{3.5}
$$

We further define the detector response or antenna pattern function:

$$
F_I^A(\hat{\Omega}, t) = d_I^{ab}(t)\, e_{ab}^A(\hat{\Omega}) ,
\tag{3.6}
$$

which encodes the directional sensitivity of detector I to a plane-polarized gravitational wave propagating in direction $\hat{\Omega}$.

Contracting (3.1) with the detector tensors d_I, the signal amplitudes in the Ith detector can be expressed in terms of the antenna pattern functions as

$$
h(t) \equiv h_I(t) = \int_{-\infty}^{\infty} df \int_{S^2} d\hat{\Omega}\, \tilde{h}_A(f, \hat{\Omega}) F_I^A(\hat{\Omega}, t) e^{i2\pi f(t + \hat{\Omega}\cdot\mathbf{x}_I(t)/c)}
\tag{3.7}
$$

3.2   Statistical properties of a SGWB

The stochastic GW background is usually described in terms of a dimensionless quantity, GW spectrum

$$\Omega_{\text{gw}}(f) := \frac{1}{\rho_c}\frac{d\rho_{\text{gw}}}{d\ln f} \ ,\tag{3.8}$$

where $d\rho_{\text{gw}}$ is the energy density of the gravitational radiation in the frequency range f to $f + df$ and ρ_c is the critical energy density follows from the Friedman equation,

$$\begin{aligned}
\rho_{\text{gw}} &= \frac{c^2}{32\pi G}\langle \dot{h}_{ab}(t,\mathbf{x})\dot{h}^{ab}(t,\mathbf{x})\rangle \ , \\
\rho_c &= \frac{3c^2 H_0^2}{8\pi G} \ ,
\end{aligned}\tag{3.9}$$

where H_0 is the Hubble expansion rate for today. Here, Ω_{gw} is not to be confused with the unit vector $\hat{\Omega}$ defined in (3.2).

For a stochastic gravitational-wave background the Fourier amplitudes of gravitational wave strain $\tilde{h}_A(f,\hat{\Omega})$ are random fields whose expectation values define the statistical properties of the background. Without loss of generality we can assume that the fields have zero mean:

$$\langle \tilde{h}_A(f,\hat{\Omega})\rangle = 0,\tag{3.10}$$

where $\langle x \rangle$ denotes mean of x. We further assume that the background is unpolarized, Gaussian and stationary. The most general form of the quadratic expectation values satisfying these requirements is

$$\langle \tilde{h}_A^*(f,\hat{\Omega})\tilde{h}_{A'}(f',\hat{\Omega}')\rangle = \mathcal{P}_A(f,\hat{\Omega})\delta(f - f')\delta_{AA'}\delta(\Omega,\hat{\Omega}') \ ,\tag{3.11}$$

where $\mathcal{P}_A(f,\hat{\Omega})$ specifies both the spectral and angular distribution of the background. Here, $\langle xy \rangle$ denotes the covariance of x and y. However, in what follows, we

17

will assume that $\mathcal{P}_A(f, \hat{\Omega})$ can be factorized into a product of two functions:

$$\mathcal{P}_A(f, \hat{\Omega}) = P_A(\hat{\Omega}) H(f) ,\tag{3.12}$$

where $H(f)$ is the two-sided GW source power spectral density (PSD). This does not amount to a loss of generality if one restricts attention to small enough frequency bands.

Thus, the directionality of the radiation is determined by the spatial function $P_A(\hat{\Omega})$ and the spectral properties of the radiation is determined by $H(f)$. This is how we model *anisotropic background* where signal to be stochastic and uncorrelated in the two polarizations, different frequencies and different sky locations. The spatial distribution function $P_A(\hat{\Omega})$ can be expanded in terms of a set of basis appropriate functions on the two sphere.

For an unpolarized background we further introduce a notation $\mathcal{P}(\hat{\Omega}) = P_+(\hat{\Omega}) = P_\times(\hat{\Omega})$. Therefore the fractional energy density in gravitational waves $\Omega_{\mathrm{gw}}(f)$ is related to the strain power spectrum through

$$\Omega_{\mathrm{gw}}(|f|) = \frac{8\pi^2}{3H_0^2} |f|^3 H(f) \int_{S^2} d\hat{\Omega} \, \mathcal{P}(\hat{\Omega}) .\tag{3.13}$$

For an *isotropic background* the directionality is set to unity, i.e., $\mathcal{P}(\hat{\Omega}) = 1$, which simplifies (3.13) by $\int_{S^2} d\hat{\Omega} \mathcal{P}(\hat{\Omega}) = 4\pi$.

The time-series of Ith detector's output $\mathcal{O}_I(t)$ is a sum of the GW signal $h_I(t)$ and the detector noise $n_I(t)$:

$$\mathcal{O}_I(t) = h_I(t) + n_I(t).\tag{3.14}$$

Statistically, the gravitational wave strain $h_I(t)$ are uncorrelated with the detector noise; that is, in the time domain the following four correlations are zero:

$$\langle h_I(t) \, n_J(t') \rangle = 0 .\tag{3.15}$$

We also assume that the noise is Gaussian with zero mean, i.e., $\langle n_I(t) \rangle = 0$ and uncorrelated in different detectors, i.e.,

$$\langle n_I(t)\, n_J(t') \rangle = 0 \; ; \quad I \neq J. \tag{3.16}$$

This assumption is not unreasonable when the detectors are widely separated across the globe.

Since the stochastic signals are unmodeled and are expected to be weak, the best strategy to detect a weak signal buried in detector noise is by correlating outputs of at least a pair of detectors. Since two gravity-wave detectors will not necessarily be either coincident or coaligned, there will be a reduction in sensitivity due to (i) the separation time-delay between the two detectors and (ii) the non-parallel alignment of the detector arms. These effects are accounted for by introducing a normalized filter function while cross-correlating the detectors' output. The filter that maximizes signal-to-noise ratio (SNR) usually depends on the spectrum of the SGWB, the noise power spectral densities of the detectors and the *overlap reduction function*, which accounts the separation time-delay and relative orientation of the two detectors. The SNR can be expressed in terms of filter function and a multiplicative factor [3]. One of the multiplicative factors is the square root of observation time. This multiplicative factor means that we can dig out a weak signal from noise by allowing a long enough observation time. The observation period could be from one sidereal day to several months.

Chapter 4

Detecting an Anisotropic Background with GW Radiometry

Radiometry or aperture synthesis is a well-known technique in radio astronomy and CMB experiments [13, 14]. The principle of earth rotation aperture synthesis can well be used for extracting the anisotropies of GW background using a pairs of GW detectors [1]. Since the noise streams in different detectors are uncorrelated, the cross correlation between the outputs from a pair of detectors with an appropriate direction dependent filter is the best statistic for the estimation of the strength of stochastic signals that can be expected to be present in those outputs.

A gravitational wave radiometer can be thought of as a pair of GW detectors separated by a distance, termed as the baseline (see Fig. 4.1). Owing to the earth's rotation, the baseline vector changes direction while keeping its magnitude fixed and hence allows a time-dependent phase delay for a particular direction of the sky. This delay corresponds to the difference between the times of arrival between two

detector sites of GW signal from that direction. The cross correlation of the data from the two detectors with appropriate time delays would cause potential GW signals interfere constructively from the same direction. Whereas signals from other directions will tend to cancel out because of destructive interference.
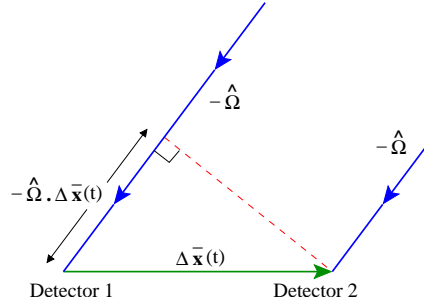

Figure 4.1: Geometry of an elementary GW radiometer [1].

In Fig. 4.1 two detectors are at locations $\mathbf{x}_I$ (where, $I = 1, 2$), and the baseline vector joining the two sites is $\triangle\mathbf{x} := \mathbf{x}_2 - \mathbf{x}_1$. The unit vector $\hat{\Omega}$ is the direction to the source, which is fixed in the barycentric frame. The phase difference $-\hat{\Omega} \cdot \triangle\mathbf{x}(t)$ between signals arriving at two detector sites from the same direction is show in the figure. The baseline vector $\triangle\mathbf{x}$ rotates with the rotation of the earth keeping its magnitude fixed. The modulation of the cross-correlation of the SGWB signals in the detector pair can be modelled for each $\hat{\Omega}$. By searching for this modulation pattern in the detectors' data one can infer the nature and sky position of the source. A map of the SGWB can be, thus, constructed by performing this synthesis for each location in the sky, patch by patch. An approximate size of the patch or resolution needed to cover the full sky can be estimated from a naive estimate $\triangle\theta \sim \lambda_{\mathrm{gw}}/(|\triangle\mathbf{x}| \sin\theta)$, where λ_{gw} is the GW wavelength and θ is the angle of incidence. So, e.g., for $\lambda_{\mathrm{gw}} = c/1000\mathrm{Hz}$, $|\triangle\mathbf{x}| = 3000\mathrm{km}$, and $\theta = 90^0$ (overhead

source), $\triangle \theta \approx 0.1$. A better estimate of the resolution follows from considerations involving the pixel-to-pixel Fisher information matrix, in which case the solid angle resolution scales inversely proportional to the square of the signal-to-noise ratio.

4.1 The cross-correlation statistic

Given a time-series $\mathcal{O}_I(t)$, we define its short-term Fourier transform $\tilde{\mathcal{O}}_I(t; f)$ by

$$\tilde{\mathcal{O}}_I(t; f) := \int_{t-\tau/2}^{t+\tau/2} dt' e^{-i2\pi f t'} \mathcal{O}_I(t') \,, \tag{4.1}$$

where τ is much greater than the light-travel time between any pair of detectors, but is small enough that the detector response function $F_I^A(\hat{\Omega}, t)$ (see Eq. (3.6)) and detector location $\mathbf{x}_I(t)$ do not vary significantly with the time over the interval $[t - \tau/2, t + \tau/2]$.

Since the targeted source is unmodeled, we search for its GW signal by looking for the same pattern in the data of two or more detectors after accounting for time-delays and detector responses consistent with a given sky location. This is done by cross-correlating the data $\mathcal{O}(t)$ from the detectors, taken in pairs, with a sky-position dependent time-frequency filter $\tilde{Q}^k(t; f)$, labeled by the sky-position index k. The cross-correlation statistic for the data $\mathcal{O}_{1,2}(t)$ from two detectors or, equivalently, for a baseline is defined as follows:

$$S^k(t) = \int_{-\infty}^{\infty} df \; \tilde{\mathcal{O}}_1^*(t; f) \tilde{\mathcal{O}}_2(t; f) \tilde{Q}^k(t; f) \,, \tag{4.2}$$

where the filter that maximizes the signal-to-noise ratio (SNR) is given by [1]

$$\tilde{Q}^k(t; f) \propto \frac{H(f) \, \gamma^*(\hat{\Omega}_k, t; f)}{P_1(t; |f|) \, P_2(t; |f|)} \,. \tag{4.3}$$

22

Here $P_{1,2}(t; |f|)$ are one-sided noise power spectral density of the two detectors. The function $\gamma(\hat{\Omega}, t; f)$ is a geometric factor that takes into account the separation time delay and relative orientation of the two detectors:

$$\gamma(\hat{\Omega}_k, t; f) = \sum_A F_1^A(\hat{\Omega}_k, t) \, F_2^A(\hat{\Omega}_k, t) \, P_A(\hat{\Omega}_k) e^{i2\pi f \hat{\Omega}_k \cdot \triangle \mathbf{x}(t)/c} \; , \tag{4.4}$$

where $\triangle \mathbf{x}(t) = \mathbf{x}_2(t) - \mathbf{x}_1(t)$ is the baseline vector. For an isotropic background, one can integrate this function over the sky, obtaining the standard *overlap reduction function* [15]

$$\gamma(f) = \frac{5}{8\pi} \int_{S^2} d\hat{\Omega} \, \gamma(\hat{\Omega}, t; f) \; . \tag{4.5}$$

The factor $5/8\pi$ is a normalization constant which guarantees that $\gamma(f) = 1$ for all frequencies for a pair of coincident and coaligned interferometer detectors with perpendicular arms.

The filter that maximizes the signal-to-noise ratio associated with this statistic is a scalar, square-integrable function on the sky and, hence, can be resolved linearly in an appropriate basis, such as a pixel basis or the spherical-harmonic basis. In the former case, k is the pixel index. In the presence of a signal, the cross-correlation statistic (4.2) is given by

$$S^k = B_{+k'}^k P_+^{k'} + B_{\times k'}^k P_\times^{k'} + n^k \; , \tag{4.6}$$

where the *beam-function* $B_{A\ k'}^k$ is analogous to the point-spread function that maps the power in the *object* (or sky) plane to that in the *image* plane, also called the dirty map [1]; n^k is the additive noise in the kth sky-position. For an unpolarized source, the beam $\mathcal{B}_{kk'}$ (see Fig. 4.2) and noise-covariance matrix $N_{kk'} \equiv \langle n_k n_{k'} \rangle$ are
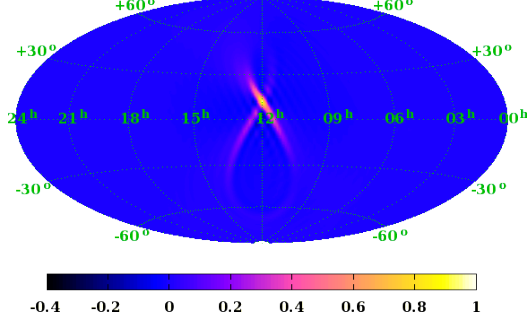
23

Figure 4.2: Illustration of a GW radiometer beam pattern at declination $+12^0$ for the LIGO detectors at Hanford and Livingston (with white noise, upper cutoff frequency of 1024 Hz, $H(f) =$ constant and observation time of one sidereal day). For low declination, the beam is shaped like the figure 8, while in the higher declination, the 8 smoothly turns into a tear drop [1].

given by:

$$
\begin{aligned}
\mathcal{B}_{kk'} &= B_{+kk'} + B_{\times kk'} \equiv \Lambda_{(k)}\mathfrak{b}_{kk'}\,, \\
&= 2\,\tau\,\Delta f\,\Lambda_{(k)} \sum_{t=0}^{T} \Gamma(\hat{\Omega}_{k'},t)\Gamma(\hat{\Omega}_{k},t)\,\Re\left[\sum_{f=f_l}^{f_u} e^{2\pi i f(\hat{\Omega}_{k'}-\hat{\Omega}_k)\cdot\Delta\mathbf{x}(t)/c}G(t,f)\right]\,, \\
N_{kk'} &= \frac{1}{4}\,\Lambda_{(k')}\,\mathcal{B}_{kk'}\,, \qquad\qquad\qquad\qquad\qquad\qquad (4.7)
\end{aligned}
$$

where $\Lambda_{(k)}$ is a filter normalization constant, $\Gamma(\hat{\Omega}_k,t)$ describes the time-varying baseline antenna-pattern, and $G(t,f)$ is a measure of the spectral strength of the

24

source relative to the baseline's noise PSDs:

$$
\begin{aligned}
\Lambda_k &:= \left[2\Delta f \tau \sum_{t=0}^{T} \sum_{f=f_l}^{f_u} G(t,f)\, \Gamma^2(\hat{\Omega}_k, t) \right]^{-1}, \\
\Gamma(\hat{\Omega}, t) &:= F_1^+(\hat{\Omega}, t) F_2^+(\hat{\Omega}, t) + F_1^\times(\hat{\Omega}, t) F_2^\times(\hat{\Omega}, t), \\
G(t,f) &:= \frac{H^2(f)}{P_1(t,f) P_2(t,f)}.
\end{aligned} \tag{4.8}
$$

The phase lag between two detectors separated by a baseline vector $\triangle\mathbf{x}(t)$, as shown in Fig. 4.1, is compensated in the filter via the phase factor $e^{(2\pi i f \hat{\Omega} \cdot \triangle\mathbf{x}(t)/c)}$ (see Eq. (4.7)). As the earth rotates this factor adjusts, so that, waves from the given direction are coherently added, while the waves from other directions tend to cancel out. The whole radiometer analysis is based on this principle.

4.2 Detection statistic

So far we have seen how to construct a cross-correlation statistic, allowing a pair of detector's outputs, for different sky locations. It is highly probable that a SGWB will be distributed across the sky. It is then natural to ask how one can combine the measurements of S^k, for all k, into a single detection statistic. Also the existence of several interferometric GW detectors across the world demands the extension of the current single-baseline analysis to a multi-baseline one.

The signal from a SGWB will typically not stand above the noise of the interferometric detectors. Only probabilities can be assigned to the presence of an expected signal. In the absence of prior probabilities, such a situation demands a decision strategy that maximizes the detection probability for a given false alarm probability. This is termed as the Neyman-Pearson criterion [16].

When the detector noise are Gaussian and uncorrelated, an assumption borne out in practice to a good approximation, the n^k are Gaussian with a non-trivial covariance matrix, $\mathbf{N}$, determined by the beam functions. If an AGWB signal, characterized by the pixel-strength vector $\vec{\mathcal{P}}$, is present in the data, then the probability density function of the radiometer output $\mathbf{S}$ is given by [1]

$$\mathfrak{P}(\mathbf{S}|\vec{\mathcal{P}}) = (2\pi)^{-N_{\text{pix}}/2} \exp[-\frac{1}{2}((\mathbf{S} - \mathbf{B} \cdot \vec{\mathcal{P}})^T \cdot \mathbf{N}^{-1} \cdot (\mathbf{S} - \mathbf{B} \cdot \vec{\mathcal{P}}) + \text{Tr}[\ln \mathbf{N}])] , \quad (4.9)$$

whereas in the absence of a signal it is

$$\mathfrak{P}(\mathbf{n}) = (2\pi)^{-N_{\text{pix}}/2} \exp[-\frac{1}{2}(\mathbf{n}^T \cdot \mathbf{N}^{-1} \cdot \mathbf{n} + \text{Tr}[\ln \mathbf{N}])] . \quad (4.10)$$

Then, by the Neyman-Pearson criterion, the optimal detection statistic is the likelihood ratio [16].

For an unpolarized background from a source distributed across multiple pixels, and quantified by the signal-strength vector $\vec{\mathcal{P}} = \vec{P}_+ = \vec{P}_\times$, the log-likelihood-ratio maximized over $\mathcal{P} \equiv \|\vec{\mathcal{P}}\|$ is:

$$\lambda = \frac{S^k (N^{-1})_{kk'} (\mathcal{B} \cdot \hat{\mathcal{P}})^{k'}}{\sqrt{(\mathcal{B} \cdot \hat{\mathcal{P}})^q (N^{-1})_{qr} (\mathcal{B} \cdot \hat{\mathcal{P}})^r}} , \quad (4.11)$$

where $\hat{\mathcal{P}} := \vec{\mathcal{P}}/\mathcal{P}$. This is our single-baseline detection statistic. The detection statistic λ has a zero mean and a unit variance in the absence of a signal. When a signal is present in the data and its parameters are matched exactly by the template's, the mean of our statistic becomes,

$$\langle\lambda\rangle = \mathcal{P}\sqrt{(\mathcal{B} \cdot \hat{\mathcal{P}})^k (N^{-1})_{kk'} (\mathcal{B} \cdot \hat{\mathcal{P}})^{k'}} . \quad (4.12)$$

The variance of the statistic remains unchanged.

26

One can extend the single-baseline detection statistic to the case of a multi-baseline network. That arises directly from maximizing relative to $\mathcal{P}$ the log-likelihood ratio for a network, and is given by

$$\lambda_{\mathcal{N}} = \frac{\sum_{\mathcal{I}=1}^{N_b} S_{\mathcal{I}}^k (N_{\mathcal{I}}^{-1})_{kk'} (\mathcal{B}_{\mathcal{I}} \cdot \hat{\mathcal{P}})^{k'}}{\sqrt{\sum_{\mathcal{I}=1}^{N_b} (\mathcal{B}_{\mathcal{I}} \cdot \hat{\mathcal{P}})^q (N_{\mathcal{I}}^{-1})_{qr} (\mathcal{B}_{\mathcal{I}} \cdot \hat{\mathcal{P}})^r}} \ , \tag{4.13}$$

where $\mathcal{I}$ is the baseline index and the subscript $\mathcal{N}$ emphasizes that this statistic is for a *Network* of baselines.

4.3 Single- and multi-baseline sensitivities

We define the single-baseline sensitivity from (4.12) as

$$\begin{aligned} \text{Sensitivity} \ &= \ \sqrt{(\mathcal{B} \cdot \hat{\mathcal{P}})^k (N^{-1})_{kk'} (\mathcal{B} \cdot \hat{\mathcal{P}})^{k'}} \ , \\ &= \ \sqrt{4 \hat{\mathcal{P}}^k \mathfrak{b}_{kk'} \hat{\mathcal{P}}^{k'}} \ , \end{aligned} \tag{4.14}$$

where $\mathfrak{b}$ is the un-normalized beam matrix [1] defined in (4.7). The sensitivity can be expressed in the spherical-harmonic basis as follows [4]:

$$\text{Sensitivity} = \sqrt{4 \mathcal{P}_{lm} \mathfrak{b}^{lm\,l'm'} \mathcal{P}_{l'm'}} \ , \tag{4.15}$$

where,

$$\mathcal{P}_{lm} = \int d\hat{\Omega} \ \hat{\mathcal{P}}(\hat{\Omega}) \, Y_{lm}^*(\hat{\Omega}) \ , \tag{4.16}$$

$$\mathfrak{b}_{lm\,l'm'} = \int\int d\hat{\Omega} \, d\hat{\Omega}' \, Y_{lm}(\hat{\Omega}) \, \mathfrak{b}(\hat{\Omega}, \hat{\Omega}') \, Y_{l'm'}(\hat{\Omega}') \ . \tag{4.17}$$

Owing to the statistical independence of the baselines, the multi-baseline sensitivity-squared is the sum of squares of the individual baseline sensitivities, as was also noted for the isotropic-background baseline sensitivities in [17]:

$$\text{Sensitivity}_{\mathcal{N}}^2 = \sum_{\mathcal{I}} \text{Sensitivity}_{\mathcal{I}}^2 \ . \tag{4.18}$$

For an unpolarized background from a single pixel, say, labeled k, and with $\hat{\mathcal{P}}^r = \delta^{r(k)}$, the sensitivity expression simplifies to

$$
\begin{aligned}
\text{Sensitivity}_{(k)} &= \sqrt{\mathcal{B}^{q(k)}(N^{-1})_{qr}\mathcal{B}^{r(k)}} = \sqrt{4\,\mathfrak{b}^{(k)(k)}} \\
&= \sqrt{\frac{1}{N_{(k)(k)}}} \; .
\end{aligned}
\tag{4.19}
$$

This shows that the baseline sensitivity squared at kth pixel is just the inverse of the variance of noise in that pixel.

4.4 Parameter accuracy

The accuracy with which the parameters describing a stochastic gravitational-wave source can be measured is assessed here using the Fisher information matrix. Fisher information matrix access the amount of information that an observable of random variable carries about unknown parameters upon which the likelihood function depends. In this section we are primarily interested in how accurately we can locate a single-pixel source.

For an unpolarized background from a single pixel, say, labeled k, and with $\hat{\mathcal{P}}^r = \delta^{r(k)}$, the single-baseline detection statistic follows from (4.11) to be:

$$
\lambda_{(k)} = \frac{S^p(N^{-1})_{pq}\mathcal{B}^q_{(k)}}{\sqrt{\mathcal{B}^r_{(k)}(N^{-1})_{rs}\mathcal{B}^s_{(k)}}} \; ,
\tag{4.20}
$$

which can be interpreted as the inner-product between the data, $\mathbf{S}$, and a unit-norm template $\hat{\mathcal{B}}_k$. Hence, the *match* [19] between the unit-norm templates for the kth

and the k'th pixels becomes

$$
\begin{aligned}
M &= \frac{\mathcal{B}^p_{(k)}(N^{-1})_{pq}\mathcal{B}^q_{(k')}}{\sqrt{\mathcal{B}^r_{(k)}(N^{-1})_{rs}\mathcal{B}^s_{(k)}}\,\sqrt{\mathcal{B}^{r'}_{(k')}(N^{-1})_{r's'}\mathcal{B}^{s'}_{(k')}}}\,, \\
&= \frac{\mathfrak{b}_{(k)(k')}}{\sqrt{\mathfrak{b}_{(k)(k)}}\,\sqrt{\mathfrak{b}_{(k')(k')}}}\,,
\end{aligned}
\tag{4.21}
$$

here the inner products are all defined in terms of $\mathbf{N^{-1}}$ and there is no sum over the bracketed indices.

Since the *match* has a maximum value of unity at $k' = k$, one can expand M in a power series as

$$
\begin{aligned}
M &\approx 1 + \frac{1}{2}\left(\frac{\partial^2 M}{\partial\Theta^\mu_{(k')}\partial\Theta^\nu_{(k')}}\right)\bigg|_{\vec{\Theta}_{(k')}=\vec{\Theta}_{(k)}}\Delta\Theta^\mu_{(k)}\Delta\Theta^\nu_{(k)}\,, \\
&= 1 - \frac{\Gamma_{(k)\mu\nu}}{\rho^2_{(k)}}\Delta\Theta^\mu_{(k)}\Delta\Theta^\nu_{(k)}\,,
\end{aligned}
\tag{4.22}
$$

where $\Gamma_{(k)\mu\nu} \equiv \Gamma_{\mu\nu}(\vec{\Theta}_{(k)})$ is the Fisher information matrix, $\rho_{(k)}$ is the signal to noise ratio in the kth pixel and $\vec{\Theta}_{(k)} \equiv \{\cos\theta_k, \phi_k\}$. The SNR in the kth pixel $\rho_{(k)}$ should not be confused with the ρ_{gw} and ρ_c define in (3.9). The error variance-covariance matrix is given by

$$
\left\langle\Delta\Theta^\mu_{(k)}\Delta\Theta^\nu_{(k)}\right\rangle = \left(\Gamma^{-1}_{(k)}\right)^{\mu\nu}\,.
\tag{4.23}
$$

The estimation error for the position measurement is given by [20]

$$
\Delta\Omega_{(k)} = 2\pi\sqrt{\left\langle(\Delta\cos\theta_{(k)})^2\right\rangle\left\langle(\Delta\phi_{(k)})^2\right\rangle - \left\langle\Delta\cos\theta_{(k)}\Delta\phi_{(k)}\right\rangle^2}\,.
\tag{4.24}
$$

For multiple baselines, the Fisher information matrix can be written as

$$
\left[\Gamma_{(k)\mu\nu}\right]_{\mathcal{N}} = \sum_{\mathcal{I}}\Gamma_{\mathcal{I}(k)\mu\nu}\,,
\tag{4.25}
$$

where $\mathcal{I}$ is the baseline index and $\mathcal{N}$ stands for *Network*. Here, $\Gamma_{\mathcal{I}(k)\mu\nu}$ is the $\mathcal{I}$th baseline Fisher information matrix as given in (4.22). And hence, the error variance-covariance matrix becomes

$$\left\langle \Delta\Theta^{\mu}_{(k)}\Delta\Theta^{\nu}_{(k)} \right\rangle_{\mathcal{N}} = \left(\left[\Gamma_{(k)}\right]^{-1}_{\mathcal{N}} \right)^{\mu\nu}. \tag{4.26}$$

So, the estimation error solid angle for locating the source in the multi-baseline is expressed as

$$\left[\Delta\Omega_{(k)}\right]_{\mathcal{N}} = 2\pi\sqrt{\left\langle(\Delta\cos\theta_{(k)})^2\right\rangle_{\mathcal{N}}\left\langle(\Delta\phi_{(k)})^2\right\rangle_{\mathcal{N}} - \left\langle\Delta\cos\theta_{(k)}\Delta\phi_{(k)}\right\rangle^2_{\mathcal{N}}}. \tag{4.27}$$

4.5   Numerical results

We now compare the sensitivities of the three baselines arising from Virgo (V1) and the two LIGO detectors at Hanford (H1) and Livingston (L1) with 4km arm-lengths. We also compare the accuracies with which a source could be located by the three baselines. The noise PSDs of all detectors are taken to be those of the corresponding design sensitivities for this analysis. In Fig. 4.3–4.6 the signal band is 40-1024Hz, with source PSD held constant, $H(f) = 1.516 \times 10^{-48}$/Hz.

In all the figures, the sky is gridded up into 768 pixels by using the Hierarchical Equal Area iso-Latitude Pixelization (HEALPix) scheme [18]. The three radiometric baselines [4] constructed from them are denoted as H1L1, H1V1 and L1V1. The triple-baseline network is termed as H1L1V1.
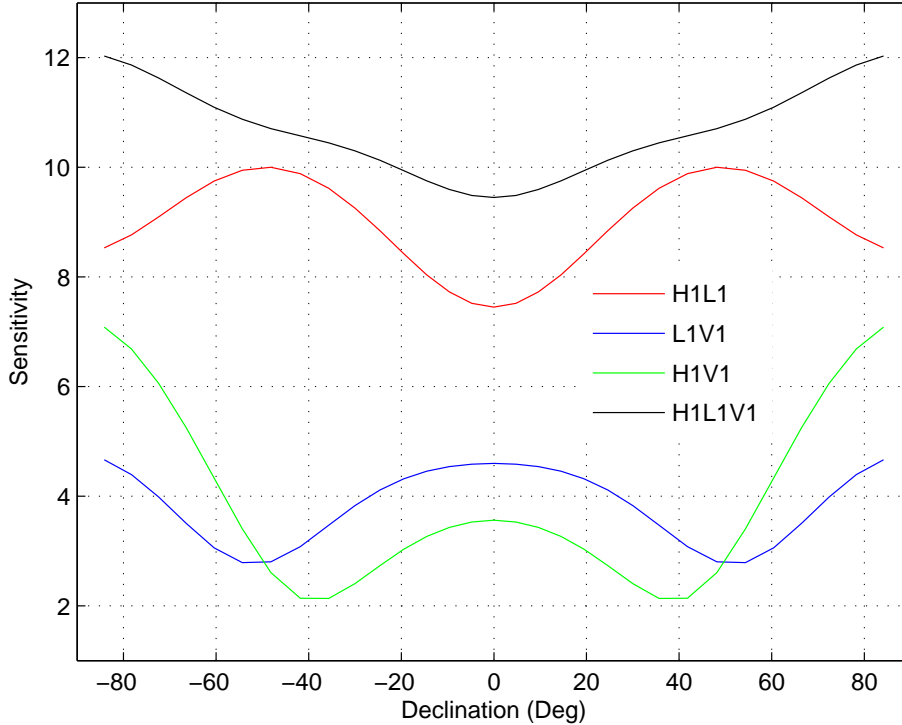
Figure 4.3: The sensitivities of three different baselines and their network are plotted as functions of the declination of a single-pixel AGWB source. The source PSD ($H(f) = 1.516 \times 10^{-48}$/Hz) is chosen such that it has maximum SNR= 10 in the H1L1 baseline. (Note that the source parameter $\mathcal{P}$ is set to unity for these plots). The signal band considered here is 40-1024 Hz.
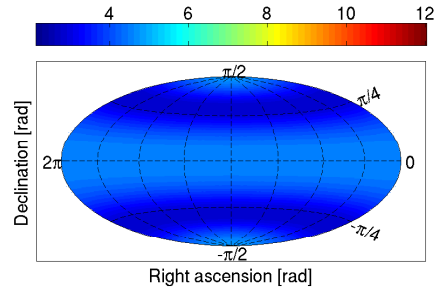
4.6 Simulations

The true power of SGWB arriving from a sky-position k is convolved with the corresponding beam response function and is given in (4.6). This can be estimated by maximizing the likelihood (4.9) with pixel-strength vector $\hat{\mathcal{P}}$, and the estimate
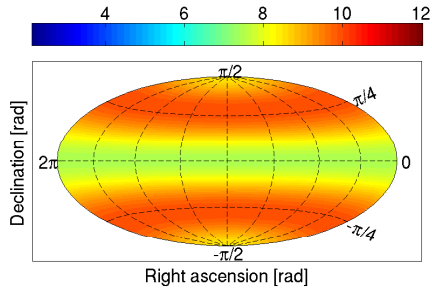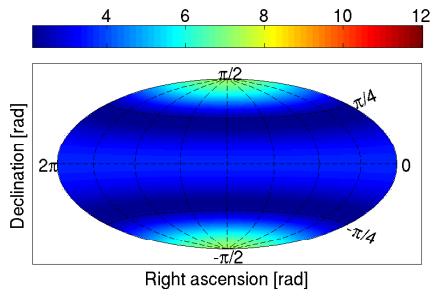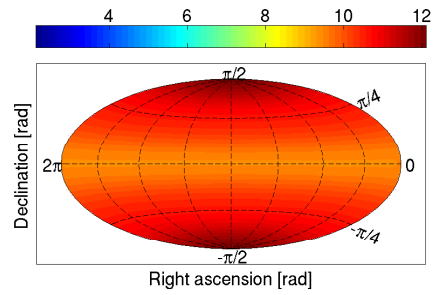
Figure 4.4: Sensitivity sky-maps for single baselines (a) H1L1, (b) L1V1, (c) H1V1, and the multi-baseline network (d) H1L1V1 for the same source and band considered in Fig. 4.3.
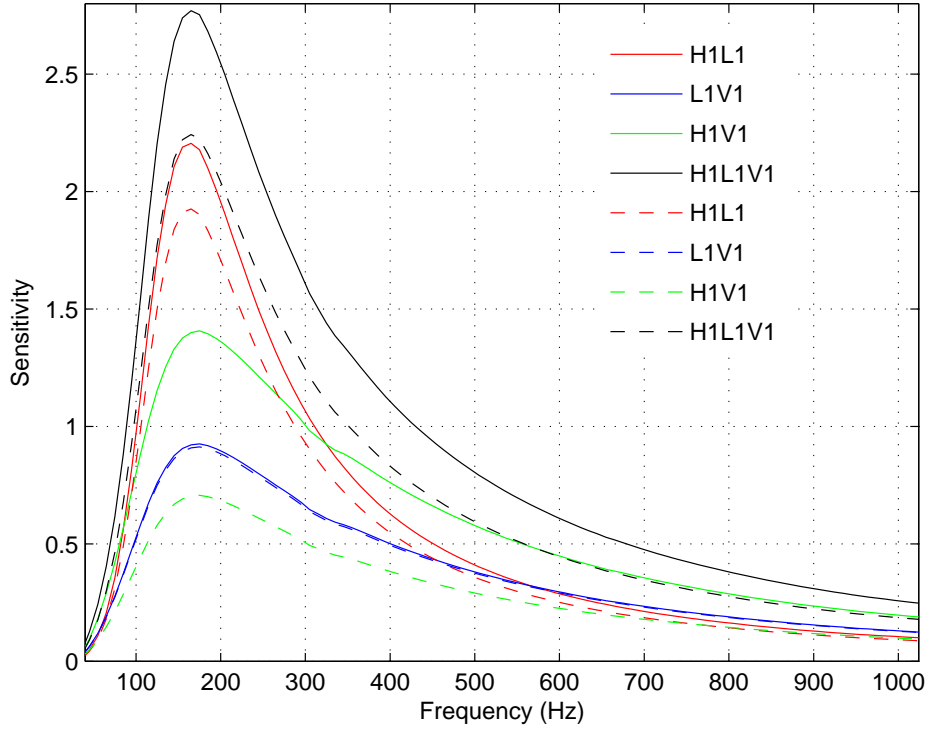
Figure 4.5: The sensitivities of three single baselines and their multi-baseline network plotted as functions of the central frequency of the source band. The source is chosen to have a constant $H(f) = 1.516 \times 10^{-48}/\text{Hz}$ and a band width of 10Hz. The solid lines represent the sensitivities at the celestial poles and the dashed lines represent those at the celestial equator.
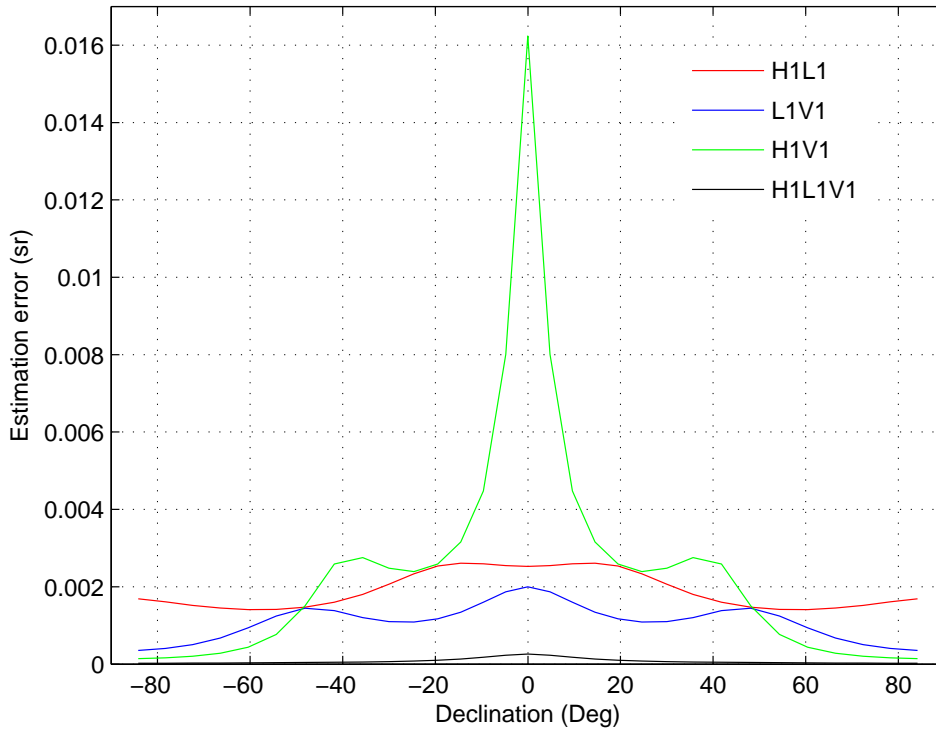
Figure 4.6: The 1σ error in the solid angle for locating a source with three single baselines and their multi-baseline network. The source and band considered here are the same as in Fig. 4.3. Note that an error of 1sr $\simeq$ 3282.80635 sq-degrees, and that the error here decreases as $1/\mathrm{SNR}^2$.

is given by [1]:

$$\check{\mathcal{P}}_k = (\mathcal{B}^{-1})_{kk'} S_{k'} \,. \tag{4.28}$$

The above relation holds also for a network of baselines.

Note that for the case of source injections we simulate data with signal using the formula [1]

$$\tilde{x}_1^*(t,f)\tilde{x}_2(t,f) = \langle \tilde{h}_1^*(t,f)\tilde{h}_2(t,f) \rangle + \tilde{n}_1^*(t,f)\tilde{n}_2(t,f)\,,$$

$$\langle \tilde{h}_1^*(t,f)\tilde{h}_2(t,f') \rangle = \delta_{ff'} H(|f|) \sum_i \mathcal{P}_i \, \gamma(\hat{\Omega}_i, t, |f|)\,. \tag{4.29}$$

To evaluate the quantity of the deconvolution, we use a constant known as the "normalized mean square error" (NMSE), expressed in terms of the injected $\mathcal{P}$ and the estimated $\check{\mathcal{P}}$ maps as

$$\mathrm{NMSE} := \frac{|\check{\mathcal{P}} - \mathcal{P}|^2}{|\mathcal{P}|^2} \,. \tag{4.30}$$

Figures 4.7–4.11 illustrate the deconvolution for couple of simulated SGWB sources. A localized polar cap and maps similar to CMB temperature anisotropy sky with galactic foreground (off the equatorial plane (EP) and in the equatorial plane) were injected as toy maps. The simulations described here are made up of one sidereal day of simulated data.
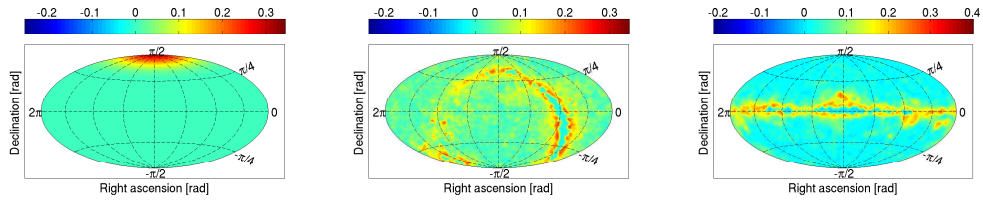
(a) Localized polar cap   (b) Diffuse source off EP   (c) Diffuse source in EP
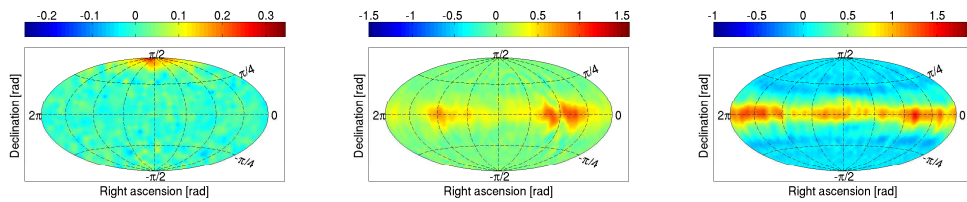
Figure 4.7: Examples of injected maps.
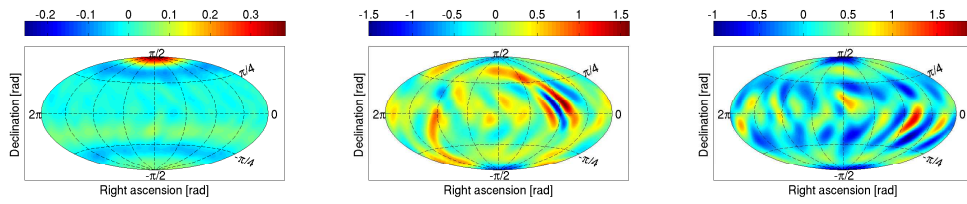
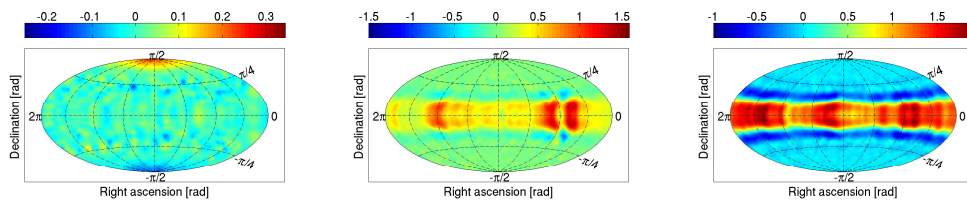(a) H1L1   (b) H1L1   (c) H1L1

(d) L1V1   (e) L1V1   (f) L1V1
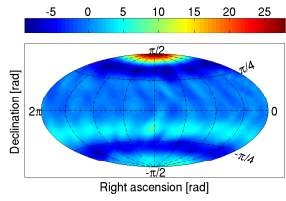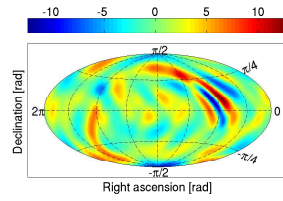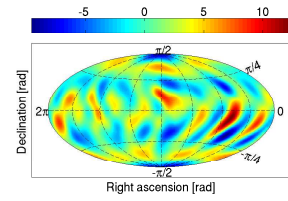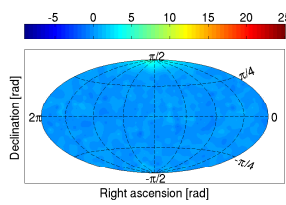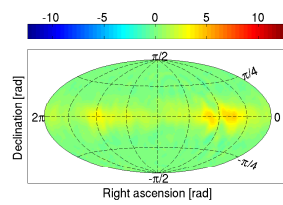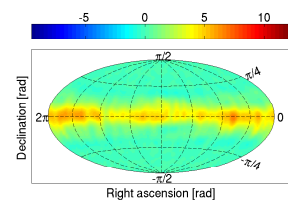
(g) H1V1   (h) H1V1   (i) H1V1

Figure 4.8: Dirty maps - made from simulated data using the radiometer analysis.

36

(a) H1L1   (b) H1L1   (c) H1L1

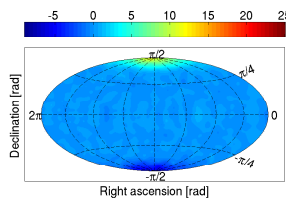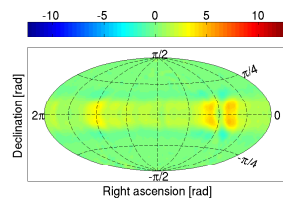(d) L1V1   (e) L1V1   (f) L1V1
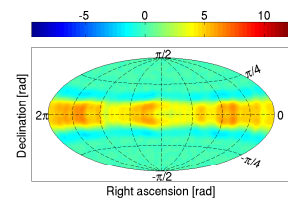
(g) H1V1   (h) H1V1   (i) H1V1

Figure 4.9: Here we plot S/σ, where S is plotted in the dirty maps of Fig. 4.8 and σ is the standard deviation of S for each pixel.

(a) H1L1 (NMSE = 1.05)   (b) H1L1 (NMSE = 0.45)   (c) H1L1 (NMSE = 0.58)

(d) L1V1 (NMSE = 0.88)   (e) L1V1 (NMSE = 0.70)   (f) L1V1 (NMSE = 0.87)

(g) H1V1 (NMSE = 1.37)   (h) H1V1 (NMSE = 0.86)   (i) H1V1 (NMSE = 0.93)
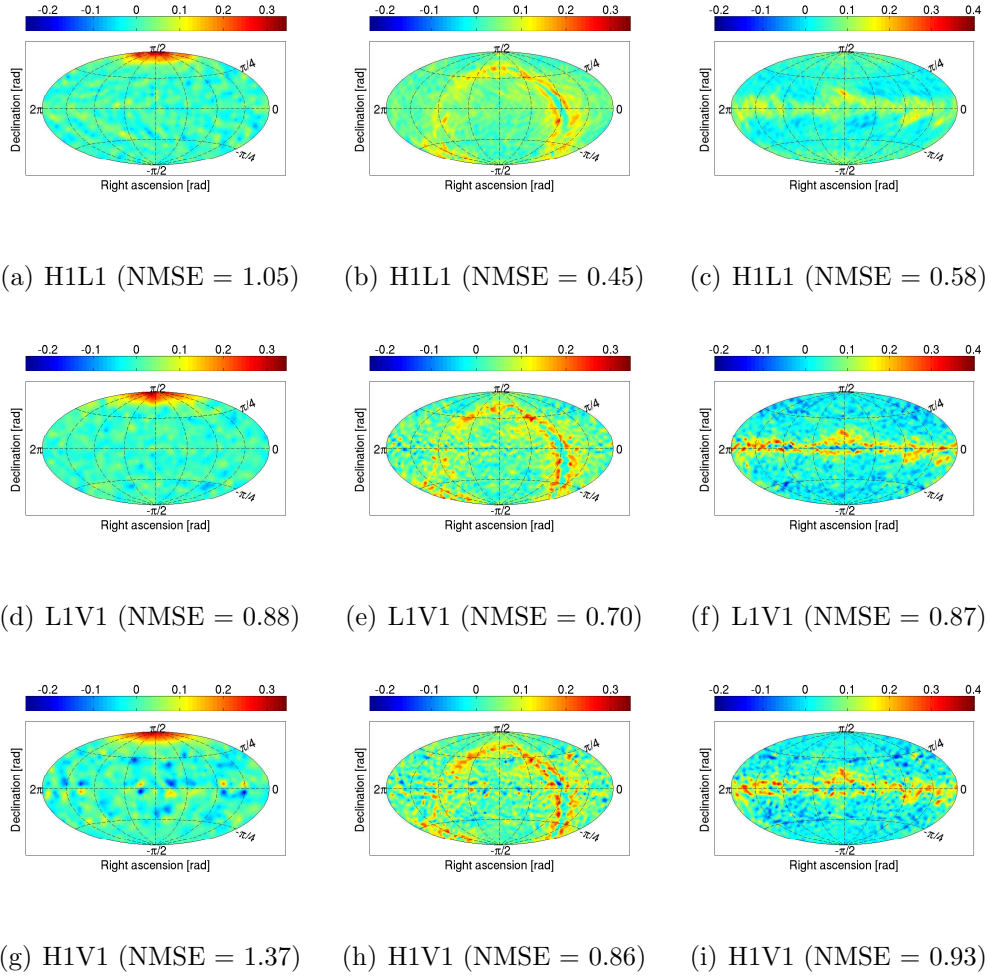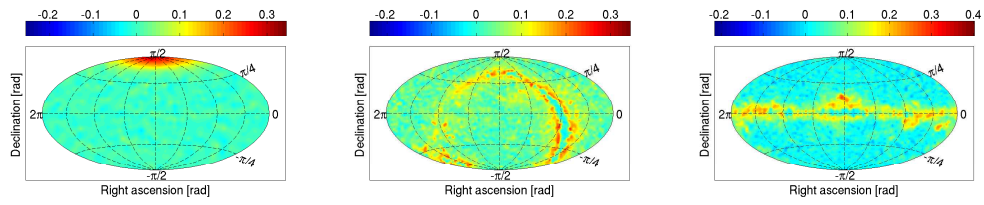
Figure 4.10: Clean maps - obtained by deconvolution of the dirty maps using 40 CG iterations.

(a) H1L1V1 (NMSE = 0.44) (b) H1L1V1 (NMSE = 0.33) (c) H1L1V1 (NMSE = 0.37)

Figure 4.11: Clean maps (Network)- obtained by deconvolution of the dirty maps using 40 CG iterations.

Chapter 5

Conclusion

The LIGO-Virgo multi-baseline network offers a sensitivity which is 5-35% better than that of H1L1-baseline. Adding Virgo to the LIGO pair helps considerably in estimating the source parameters (e.g., localizing the sky-position better by a factor of 10). This improvement of network sensitivity merits the investment required for extending the current single-baseline analysis [1, 2] to a multi-baseline one. This conclusion is strengthened by the fact that adding a detector to a baseline can potentially mitigate the contribution of cross-correlated environmental noise that affects only one of the three resulting baselines. Including V1, which is on a different continental plate than the H1L1 baseline, can serve this purpose. Employing a null-stream [24] statistic to complement the detection statistic might also help in discriminating against such noise.

The three interferometers, two LIGO and Virgo, suitable for making a GW radiometer network have reached their designed sensitivity and are acquiring since data. Single baseline radiometry analysis tools already exist since S4. Extending

them to do a multi-baseline analysis is straightforward. We are working on developing the necessary post-processing tools and demonstrating their functionality on LV data from S5 soon.

Appendix A

Definitions of Acronyms

AGWB: Astrophysical Gravitational Wave Background

CG: Conjugate Gradient

CMB: Cosmic Microwave Background

EE: Einstein Equation

EP: Equatorial Plane

GR: General Relativity

GW: Gravitational Wave

HEALPix: Hierarchical Equal Area iso-Latitude Pixelization

LIGO: Laser Interferometer Gravitational-wave Observatory

LMXB: Low-Mass X-ray Binary

ML: Maximum Likelihood

NMSE: Normalized Mean Square Error

PSD: Power Spectral Density

SGWB: Stochastic Gravitational Wave Background

SNR: Signal-to-Noise Ratio

TT: Transverse-Traceless

H1: The LIGO detector with 4km arm-length at Hanford

L1: The LIGO detector with 4km arm-length at Livingstone

V1: The "European gravitational (wave) observatory" with 3km arm-length at Cascina

H1L1: The baseline constructed from H1 and L1

L1V1: The baseline constructed from L1 and V1

H1V1: The baseline constructed from H1 and V1

H1L1V1: The triple-baseline network constructed from H1, L1 and V1

S4: The fourth LIGO science run

S5: The fifth LIGO science run

Bibliography

[1] S. Mitra, S. Dhurandhar, T. Souradeep, A. Lazzarini, V. Mandic, S. Bose and S. Ballmer, Phys. Rev. D **77**, 042002 (2008).

[2] Stefan W. Ballmer, Class. Quant. Grav. **23**, S179 (2006).

[3] B. Allen and J. D. Romano, Phys. Rev. D **59**, 102001 (1999).

[4] S. Ballmer, S. Bose, V. Mandic, S. Mitra, J. D. Romano, D. Talukder and E. Thrane, *Probing the anisotropies of a stochastic gravitational-wave background using a network of ground-based laser interferometers*, to be submitted for publication in Phys. Rev. D.

[5] D. Coward and T. Regimbau, New Astron. Rev. **50**, 461-467 (2006).

[6] B. F. Schutz, *A first course in general relativity* (Cambridge University Press, 1985).

[7] P. R. Saulson, *Fundamentals of Interferometric Gravitational Wave Detectors* (World Scientific, 1994).

[8] T. Regimbau and J. A. de Freitas Pacheco Astron. Astrophys. 376, 381-385 (2001).

[9] A. A. Starobinsky, JETP Lett. **30**, 682 (1979).

[10] T. Kahniashvili, A. Kosowsky, G. Gogoberidze and Y. Maravin, *Detectability of Gravitational Waves from Phase Transitions* [arXiv:astro-ph/0806.0293].

[11] B. Allen, *The stochastic gravity-wave background: sources and detection* [arXiv:gr-qc/9604033].

[12] C. Cutler, K. S. Thorne, *An Overview of Gravitational-Wave Sources* [arXiv:gr-qc/0204090].

[13] B. F. Burke and F. Graham-Smith, *An Introduction to Radio Astronomy* (Cambridge University Press, 1997).

[14] R. B. Partridge, *3K: The Cosmic Microwave Background Radiation* (Cambridge University Press, 1995).

[15] E. Flanagan, Phys. Rev. D **48**, 2389 (1993).

[16] C. W. Helstrom, *Statistical Theory of Signal Detection* (Pergamon, London, 1968).

[17] G. Cella, C. N. Colacino, E. Cuoco, A. Di Virgilio, T. Regimbau, E. L. Robinson and J. T. Whelan, Class. Quant. Grav. **24**, S639 (2007).

[18] See, e.g., http://healpix.jpl.nasa.gov/ .

[19] Benjamin J. Owen, Phys. Rev. D **53**, 6749 (1996).

[20] C. Cutler, Phys. Rev. D **57**, 12 (1998).

[21] See, e.g., http://www.ligo.caltech.edu/ .

[22] See, e.g., http://www.virgo.infn.it/ .

[23] See, e.g., http://www.ligo.org/ .

[24] Y. Gürsel and M. Tinto, Phys. Rev. D **40**, 3884 (1989).